Computational Materials Science 147 (2018) 7–17

Contents lists available at ScienceDirect

Computational Materials Science

journal homepage: www.elsevier.com/locate/commatsci

An interatomic potential for simulation of defects and phase change of zirconium

Yifang Ouyang [a,*], Jizheng Wu [a], Minghui Zheng [a], Hongmei Chen [a], Xiaoma Tao [a], Yong Du [b], Qing Peng [c,*]

[a] Guangxi Colleges and Universities Key Laboratory of Novel Energy Materials and Related Technology, College of Physical Science and Technology, Guangxi University, Nanning 530004, China
[b] State Key Laboratory of Powder Metallurgy, Central South University, Changsha 410083, China
[c] Department of Nuclear Engineering and Radiological Science, University of Michigan, Ann Arbor, MI 48109, USA

ARTICLE INFO

Article history:
Received 13 December 2017
Received in revised form 24 January 2018
Accepted 25 January 2018

Keywords:
Embedded atom method (EAM)
Zirconium
Phonons
Point defects
Phase transformations

ABSTRACT

We introduce a long-range interaction analytical embedded atom method (namely la-EAM) interatomic potential, which has been developed by fitting the lattice constants, cohesive energy, mono-vacancy formation energy and elastic constants of α-Zirconium. We validate this la-EAM potential by extensive investigation of the bulk, surface, and defect properties of Zirconium using molecular dynamics simulations compared with available experiments and theoretical results. We examine the lattice constants, cohesive energy, elastic constants, phonon dispersion curves of α-, β-, and ω-Zirconium and find a good agreement with available experiments. We have studied the 0D (zero-dimension) defects including vacancies and self-interstitial atoms, 1D defects (dislocations), 2D defects including surface and stacking fault, and 3D bulk properties. Furthermore, our phase transformation energy barrier of $\alpha \rightarrow \omega$ agrees with the experimental observation. The success of our potential could attribute to the correctly accounting for the long-range interactions of the Zr atoms. Our results suggest that the developed la-EAM potential of Zr is useful in molecular dynamics simulations of bulk, surface and defect properties and phase transitions of Zirconium at various temperatures and pressures.

1. Introduction

Zirconium is a fascinating *d*-orbital transition metal, which has extensive technical applications in aerospace, medical and nuclear fields due to its high strength, light weight, corrosion resistance, and small neutron absorption sections [1]. At ambient conditions, the crystalline structure of Zirconium is hexagonal close-packed (hcp) structure, or α phase. When the temperature rises, at zero pressure, Zirconium transforms from martensitic (a face-centered cubic, fcc) structure into the body-centered cubic (bcc) structure, or β phase, at 1136 K, and then eventually melts. When the pressure is increased while temperature kept at room temperature, a martensitic phase (fcc) transformation into the ω phase is observed [2,3]. The ω phase is widely accepted as the strengthening phase in Zr and its alloys due to its higher hardness over α phase [4].

The phase transformation of Zirconium may be explained by its anomalism of the phonon dispersion curves. One of the aims of this work is the anomalous phonon properties for Zirconium, which might be a hint to the various martensitic transformations. Furthermore, it could provide some hint in understanding the anomalous self-diffusion of Zirconium. In the hcp structure, the zone center of the [0 0 1] LO branch substantially softens and exhibits a dip at low temperature [5]. This may lead to the superconducting transition. The phonon dispersion curves of bcc phase show that there is a large low-energy dip in the high-symmetry longitudinal phonon branch *L* [ξξξ] for ξ=2/3. This dip appears at high temperature, and it is temperature-dependent. This soft mode is believed to cause the $\alpha \rightarrow \omega$ phase transformation. The entire T_1 [ξξ0] phonon branch with [1 $\bar{1}$ 0] polarization is of low energy and is overdamped, which is related to the transformation of $\beta \rightarrow \alpha$. There is inconsistency of phonon-dispersion curves of bcc phase between the theoretical predictions and experiments. At ambient pressure, the theoretical predicted soft modes of T_1 *N*-point phonon and an unstable bcc structure [6], while, experiments confirmed the phase transformation occurs at a finite frequency [7].

From experimental aspect, the orientation relationship of phase transformation between the parent and the product phases may be determined. However, such an approach may result in multiple transformation pathways for a given set of orientation relationships. As a consequence, one has to guess the possible

* Corresponding authors.
E-mail addresses: ouyangyf@gxu.edu.cn (Y. Ouyang), qpeng.org@gmail.com (Q. Peng).

https://doi.org/10.1016/j.commatsci.2018.01.049
0927-0256/

transformation pathway by calculating the energy barrier of phase transformation to unravel the mechanism of phase transition [8,9].

Molecular dynamics (MD) and Monte Carlo (MC) methods are powerful techniques for atomistically investigating the phenomena relevant to temperature and time dependence in large scales, which in general are impractical for first-principles methods. The force field potential describes the atomistic interactions between atoms, which plays an essential role in MD and MC simulations. However, the accuracy of atomistic simulation ultimately depends on the force field potentials, which is generally generated by fitting with experiments or first-principles calculations. Plenty of empirical potentials have been developed in the past six decades (refer to [10,11]).

Zirconium has been the subject of many theoretical studies. There have been quite a lot of attempts to develop many-body interatomic potentials for the hcp structures of various materials, especially for Zr. These potentials, most of them if not all, aim to reproduce the experimental values of elastic constants and c/a ratio of hcp structures. There are five independent elastic constants of hcp structures. The c/a ratio of an "idea" hcp structure is 1.633. The lattice constants and elastic constants are critical important in determine many other related physical properties including modulus, strength, and hardness. It turns out that force field generated in this way can be reliable in studying the bulk, surface and defects properties. Same strategies are employed in the development of the embedded atom method (EAM) [12], as well as the n-body potential [13]. Following the schedule of EAM, Oh and Johnson [14,15] proposed an analytical EAM (AEAM) by fitting the Voigt bulk and shear moduli, with ideal c/a ratio for Mg, Zr and Ti [14] and a more realistic c/a ratio for Zr [15]. Igarashi et al. [16] presented EAM type potentials for a number of hcp metals by attempting to exactly match those properties. Hu et al. proposed an analytic modified EAM for hcp metals by including a modified term [17]. Baskes and Johnson [18,19], Kim et al. [20] presented so called modified EAM (MEAM). As for hcp structure metals, other potentials [21–23] have been developed by different means. These developed potentials have been applied to study the bulk, surface, defect and thermodynamic properties. Despite extensive efforts, an accurate force field for Zr is still lacking to describe defective structures and phase transitions. For example, the investigations of stacking fault energy in α Zirconium indicate that the long-range interaction potential is needed for exactly description of anomalous behavior of Zirconium, which, however, are missing for currently available force fields of Zr.

In this work, we develop a long-range interaction analytical EAM potential, namely la-EAM, for Zirconium by fitting the physical properties of α-Zr from experiments. The presented potential is employed to study the bulk (3D) properties, point defects (0D) properties, line defects (1D) properties, stacking fault (2D) properties, of α-Zr. In addition, we have calculated the phase transformation energy barriers. Our results are compared with literature to validate our la-EAM potential. The uniqueness of this newly developed potential is the capability to accurately model the phase transitions and various defective structures of zirconium. The organization of this work is as follows: Section 2, we introduce the la-EAM potential and details of our models and simulations. The results and discussion are presented in Section 3, followed by the conclusions in Section 4.

2. The formula of long-range analytical EAM potential

Within the framework of Embeded Atom Model (EAM), the energy of an atom in a system can be expressed as [12]

$$E_i = F_i(\rho_i) + \frac{1}{2}\sum_{j(\neq i)}\phi(r_{ij}) \tag{1}$$

where $F_i(\rho_i)$ is the embedding energy required to place an atom at site i with electron density ρ_i. $\phi(r_{ij})$ is the pair-potential between atoms i and j, and r_{ij} is the separation distance related to the specified pair of atoms i and j. ρ_i denotes the host electron density at the site of atom i which has the pair-wise contributions from each of all other atoms. This host electron density is the sum of the electron density $f(r_{ij})$ of the individual atom j with the linear superposition approximation, as

$$\rho = \sum_{j\neq i} f(r_{ij}) \tag{2}$$

Following the la-EAM scheme [24], we have fixed analytical from of $F(\rho)$, $\phi(r)$ and $f(r)$ as following.

$$F(\rho) = \begin{cases} \sum_{i=0}^{4} F_{1i}(\rho-\rho_1)^i & \rho \leqslant \rho_1 = 0.85\rho_e \\ \sum_{i=0}^{4} F_{2i}(\rho-\rho_2)^i & \rho_1 < \rho \leqslant \rho_2 = 1.0\rho_e \\ \sum_{i=0}^{3} F_{3i}(\rho-\rho_2)^i & \rho > \rho_2 \end{cases} \tag{3}$$

$$\varphi(r) = \begin{cases} -\varphi_e\left[1+\alpha\left(\frac{r}{r_1}-1\right)\right]\exp\left[-\delta\left(\frac{r}{r_1}-1\right)\right] & r \leqslant r_1 \\ \sum_{i=0}^{8}\lambda_i\left(\frac{r}{r_2}-1\right)^i & r_1 < r \leqslant r_b \\ \sum_{i=0}^{5}\kappa_i(r-r_b)^i & r_b < r \leqslant r_c \end{cases} \tag{4}$$

$$f(r) = f_e\left(\frac{r}{r_1}\right)^2 \exp\left[-\beta\left(\frac{r}{r_1}-1\right)\right] \tag{5}$$

Having specified the functions of $F(\rho)$, $\phi(r)$ and $f(r)$, the parameters were determined by fitting to experimental data. The experimental thermodynamic data including the equilibrium lattice constants a and c, elastic constants C_{11}–C_{12}, C_{44} and bulk modulus B, cohesive energy E_c, the mono-vacancy formation energy E_f were used in the present model. The parameters of pair potential are obtained by fitting the vacancy formation energy, equilibration condition, elastic constants C_{11}–C_{12} and C_{44}.

With the developed la-EAM potential, we do further investigations using molecular static and molecular dynamics simulations using the program GULP [25]. In the calculations, the lattice parameters, elastic properties are obtained in three-dimensional (3D) periodic crystal cells. The surface energies are calculated with 15 layers with more than 10 Å vacuum layer. The formation energies were calculated using supercells $15a \times 15a \times 10c$ (α), $15a \times 15a \times 15a$ (β) and $15a \times 15a \times 20c$ (ω). The melting temperature was obtained by NPT with supercell of $30a \times 30a \times 20c$ and the atomic displacement of edge dislocation by NVT with supercell of $100a \times 3b \times 100c$ ($b = \sqrt{3}a$). The time step is 1.0 fs. The cutoff for force is 5.984 Å.

3. Results and discussion

3.1. Parameters of la-EAM potential

The la-EAM potential by fitting the formula to the experimental data. The atomic density distribution function, β is taken from Reference [26] and f_e is determined from atomic volume Ω, bulk modulus B and cohesive energy E_c as $(9\Omega B/E_c)^{0.6}$ [24]. And then the parameters ρ_1 and ρ_2 are determined from ρ_e using Eq. (2) including the 5th neighbors. The embedding function was divided into three segments, and the second segment was fitted to

Table 1
The EAM parameter for Zr (units: F_e (eV), ρ_i (Å^{-3}), r_i, r_b and r_c (Å), λ_i and K_i (eV), others (dimensionless)).

Paras.		Paras.	
f_e	0.3739748	δ	5.982360
β	1.8503693	r_1	3.192996
ρ_1	4.295063	λ_0	−0.120938606560230
ρ_2	5.053016	λ_1	0.626805682710710
F_{10}	−4.50315	λ_2	−1.12410270390263
F_{11}	−0.18568	λ_3	2.0171469277E+2
F_{12}	0.281366	λ_4	−3.117817861E+3
F_{13}	0.177704	λ_5	1.988367047E+4
F_{14}	0.0370108	λ_6	−6.406638793E+4
F_{20}	−4.55000	λ_7	1.0310670762E+5
F_{21}	0.000000	λ_8	−6.577700302E+4
F_{22}	0.0357929	r_2	4.30136474
F_{23}	−0.0127642	k_0	4.58147193739E−3
F_{24}	0.0628233	k_1	−8.67979431765E−3
F_{30}	−4.550000	k_2	2.12733895551E−2
F_{31}	0.000000	k_3	−0.541670518761980
F_{32}	0.0357929	k_4	1.95724788283577
F_{33}	0.000159553	k_5	−1.94843015108457
Φ_e	0.2497642	r_b	5.597988
α	8.247177	r_c	5.984048

experimental values. Namely, the parameters F_{20} are determined by difference between the cohesive energy and monovacancy formation energy ($E_c - E_f$), parameters F_{21} and F_{23} are equal zero, $F_{22} = (9\Omega B - 15\Omega G)(\rho_e/\rho')^2$ and $F_{24} = 30\Omega G/(E_c - E_f)$ (where G is shear modulus). The other parts of embedding function are connected smoothly with the second part, and the first part was conditioned with the value is zero when the ρ is equal to zero.

As for the pair potential, it was also divided into three segments. The first and second parts of pair potential including 15 parameters. They are optimized to minimizing the deviations of the predicted values from experiments. The third part of pair-potential was connected with the second part and reached to zero smoothly at the cut off distance. The obtained parameters are listed in Table 1. The atomic electronic density distribution function, pair-potential and embedding function of the present la-EAM for Zr are depicted in Fig. 1.

3.2. Static properties of α-, β-, ω- and fcc-Zr

The calculated lattice constants and elastic constants for α-Zr are displayed in Table 2. The present la-EAM potential reproduced exactly the lattice constants. There are a lot of theoretical studies from empirical potentials [14,15,18,20–23,27–29], first-principles [30–35] and experimental data [18,36–41] for α-Zr. The calculated lattice constant for a ranges from 3.187 to 3.237 Å, and for c from 5.045 to 5.247 Å. The present potential reproduces the lattice constants exactly. The elastic constants and their combinations of C_{11}–C_{12} and bulk modulus, B were useful in determining the potential parameters. As a result, one can expect that the calculated C_{11}, C_{12}, C_{44} and B are in good agreement with the experiments [38–40]. The elastic constant C_{44}, in particle, is exactly reproduced. Our c/a ratio, C_{13}, C_{33} and shear modulus G are also coincident with the experimental values [38,39]. The success of our potential could attribute to the correctly accounting for the long-range interactions of the Zr atoms. The comparison with the calculated elastic constants from first-principles and empirical potentials are summarized in Table 2. The other theoretical elastic constants are scattering from the experiments. The calculated static properties of α-Zr indicate that the present la-EAM potential reasonably reproduces the elastic constants of α-Zr.

In order to gain insights into the effect of pressure, the lattice constants and volume of crystalline cell under different pressure were calculated and depicted in Fig. 2. One can see that the present calculated change of lattice constants and cell volume with pressure is in good agreement with those of experiments at temperature of 298 K [36,37]. The calculated melting temperature of α-Zr

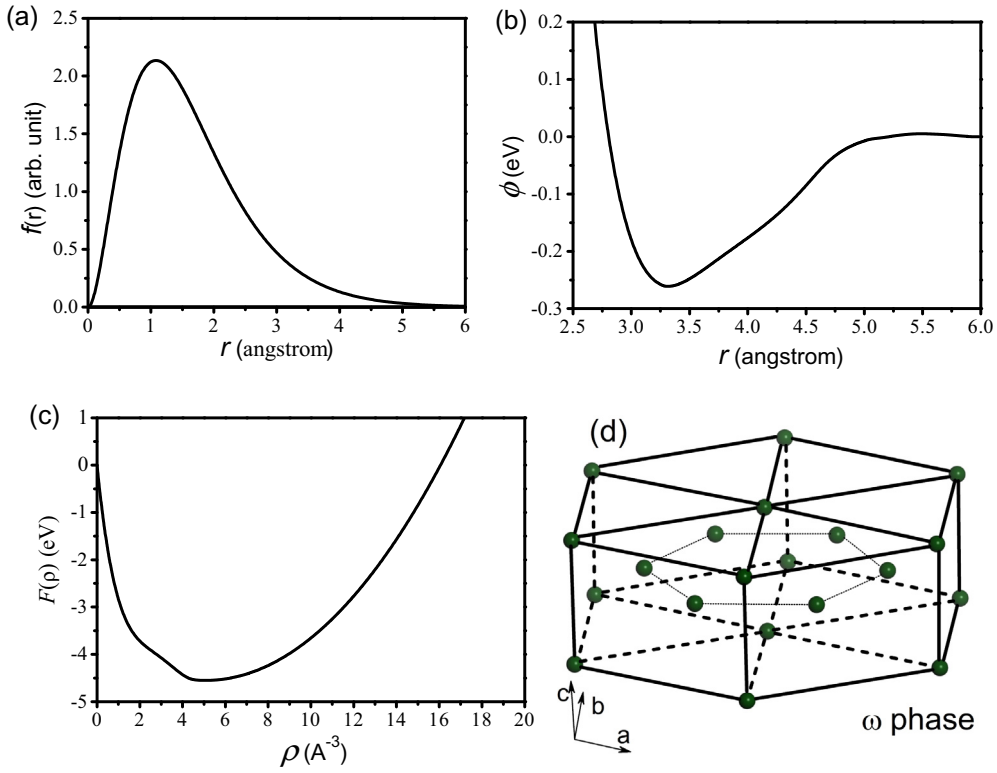

Fig. 1. The la-EAM functions for Zr: (a) the atomic electronic density distribution, (b) pair potential, (c) embedding function and (d) crystal structures of ω-Zr.

Table 2
The calculated lattice constants (in Å), cohesive energy and mono-vacancy formation energy (in eV), elastic constants and elastic moduli (in GPa) of α-Zr.

Methods	a	c	E_c	E_f	C_{11}	C_{12}	C_{13}	C_{33}	C_{44}	B	G	Ref.
Empirical potential	3.232	5.182	6.25	1.70	155.2	75.0	62.6	164.8	36.3	97.3	40.5	Present
	–	–	–	1.36	158.9	70.3	61.0	173.0	34.4	–	–	14
	–	–	6.25	1.86	147.9	66.3	66.2	182.7	39.2	–	–	15
	–	–	6.25	1.63	164.4	72.2	60.2	161.8	33.6	–	–	15
	3.237	5.153	6.3705	1.93	152	74	63.2	153.3	33.2	95.2	–	18
	3.231	5.125	6.364	2.09	151.5	71.8	66.1	160.6	34.1	96.8	–	20
	3.232	5.148	6.25	1.74	143	72.8	65.3	164.7	32.0	–	–	21
	3.232	5.148	6.249	1.976	156.8	67.4	62.9	170.3	39.5	85.4	–	22
	3.23	5.15	6.25	1.75	121.4	59.5	78.4	219.3	49.9	99.4	–	23
	3.220	5.215	6.469	2.310	165	65	63	180	48	–	–	27
	3.234	5.168	6.635	1.762	147	69	74	168	44	–	–	27
	3.2196	5.247	6.17	2.14	154	70	65	–	34	97	–	28
	3.202	5.218	6.17	–	162	77	65	–	42.5	101	–	28
	3.249	5.189	6.25	1.786	150	85	67	175	36	–	–	29
First-principles	3.236	5.168			146.7	68.5	71.3	163.3	26.0	96.0		6
	3.187	5.045			156	65	76	182	25			30
	3.234	5.152			133	80	73	148	7			30
	3.224	5.239			142	71	71	147	8			30
	3.232	5.182			139.4	71.3	66.3	162.7	25.5			31
					145.3	67.3	69.5	166.1	24.3	95.3		32
					153.0	56.8	64.8	165.7	26.1			33
	3.15	5.087			135			180	21	105		34
	3.23	5.168			146			156	28	94		34
	3.238	5.178			142.2	70.3	69.6	159.8	26.5	95.8	32.9	35
Exp.				1.70*								18
	3.232*	5.182*										36
	3.231	5.148	6.25*									37
					155.4*	67.23*	64.6	172.0	36.3*	97.34	42.5	38
					143.4	72.8	65.3	164.8	32.0			39
										92		40

* The values are used for fitting to determine the potential parameters.

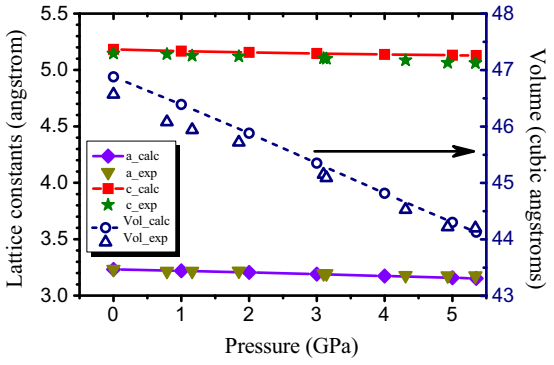

Fig. 2. The lattice constants and unit-cell volume of α-Zr as a function of pressure. The experimental data taken from Ref. [40] (the lines for guide the eye).

is 1859 K, which is some lower than that (1913 K) of Mandelev et al. [27], and that (1957 K) of Kim et al. [20] and experimental melting temperature (2128 K) [41]. This melting temperature is fictitious because α-Zr transforms to β-Zr before melting.

It is interesting to compare static properties of the β phase calculated by the present potential with experimental values at temperatures larger than the α-β experimental transformation temperatures. The results are summarized Table 3. As expected, the enthalpy difference between the β and α phase, $H_\beta - H_\alpha$ = 0.042 eV, is positive and remarkably close the experimental value at T^{tr} ($H_\beta - H_\alpha$ = 0.04 eV) [38]. The calculated lattice constant of β-Zr agrees with the experimental value [40]. We find reasonable agreement for elastic constants C_{11} and C_{12}, but an unsatisfactory for C_{44}. It is instructive to compare the shear moduli C', which is relative to the instability of the β phase and the mechanism of the phase transformation. The C' is predicted to be 6.1 GPa from

Table 3
The calculated lattice constants (in Å), cohesive energy and mono-vacancy formation energy (in eV), elastic constants and elastic moduli (in GPa) of β-Zr.

Methods	a	E_c	E_f	C_{11}	C_{12}	C_{44}	B	G	Ref.
Empirical potential	3.639	6.208	1.138	129.7	117.4	64.5	121.5	27.3	Present
	3.580			118.2	92.6	68.8	101.1		20
	3.615	6.188		106.2	101.1	73.1	102.8		23
	3.562	6.417		96	109	42			27
	3.576	6.532		50	94	50			27
	3.595	6.21		101.1	99.7	65.6	100.2		28
First-principles	3.574			86.6	92.3	26.6	90.2		6
	3.469								30
	3.580			84.2	91.4	32.3			31
	3.577			81.8	94.3	30.2	89.7		32
	3.580			108.7	85.4	10.6			42
Exp.	3.574			104	93	38	97		7
	3.627						66		40
		6.29							43

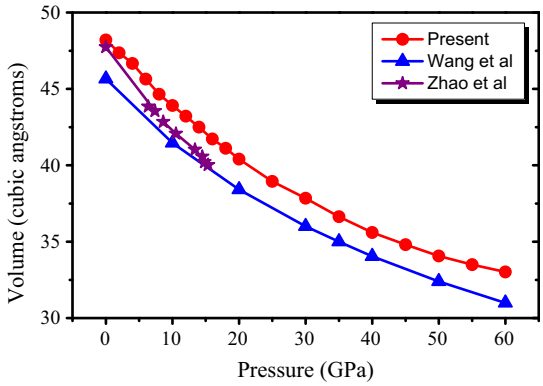

Fig. 3. The variation of unit-cell volume with pressure for β-Zr. The experimental data taken from the Zhao et al. at temperature 973 K [40] and first-principles [6].

our la-EAM, in a good agreement with the experimental value of 5.5 GPa [40]. The first-principles [6,30–32] predict $C_{11} < C_{12}$ (in Table 3), indicating a mechanically unstable β phase, opposite to the empirical potentials calculations [20,23,27,28]. Some theoretical [42] and experimental [7] studies indicate the stability of β phase. The calculated cohesive energy is coincident with that of experiment [43]. The difference of the calculated bulk moduli and experimental values is evident. This discrepancy could attribute to the different temperature used in our model. The dependence of crystal cell volume on the pressure was predicted and given in Fig. 3, with reasonable agreement with the experiment [40] and a previous theoretical prediction [6]. Under low pressure, our prediction is more accurate than the compared theoretical method [6].

It is experimentally confirmed that the face-centered cubic (fcc) structure of Zr is a metaphase [42]. The properties of fcc phase are also calculated and displayed in Table 4 along with available results of first-principles calculations [32,42] and experiment [44]. The predicted lattice constants are in line with the results from first-principles [32,42], but slightly small than that of experiment [44]. The elastic constants are in good agreement with those of first-principles [32,42].

The high-pressure phase of Zr is so called ω phase. The calculated properties for ω phase are shown in Table 5. The calculated lattice constants and elastic properties are reasonable accordant with those of first-principles [6,33,45,46] and experiment [36,40,47]. Our calculated elastic constants imply that the ω Zr is mechanically stable under pressures, because they are compliant to the mechanical stability criteria of hexagonal crystals as follows.

$$C_{44} > 0, C_{11} > |C_{12}|, (C_{11} + C_{12})C_{33} - 2C_{13}^2 > 0 \quad (6)$$

The variation of crystal cell volume and lattice constants with pressure for ω phase was depicted in Fig. 4. There is evident difference of lattice constant a between the calculation and experiment. The lattice constant c agrees well with that of experiment as the pressure increases.

3.3. Phonon dispersion

The phonon dispersion curves for α-Zr are calculated with the developed la-EAM potentials. The phonon dispersion spectrum was obtained by calculating the force constant matrix from the present la-EAM potentials by using program GULP [26]. Our calculated phonon dispersion spectra are shown in Fig. 5 with comparison to the experimental measurement [5]. As expected, we have excellent agreement for the small wave-vector acoustic phonons, because they are closely related to the elastic constants, which are included in the fitting procedure. The major discrepancy is observed for the branches issued from the high-symmetric Γ point phonon, i.e., the [0 0 1] LO, and [1 0 0] $TO_{\perp}$, and [1 1 0] $TO_{\perp}$, as shown in Fig. 5. The anomalous experimental behavior of these branches is attributed to the detailed topology of the band structure near the Fermi energy [48]. The same discrepancy has been observed by Igarashi [16] with F-S potential and by Willaime [28] using EAM model, and that calculated by tight binding [30].

Table 4
The calculated lattice constants (in Å), cohesive energy and mono-vacancy formation energy (in eV), elastic constants and elastic moduli (in GPa) of fcc-Zr.

Methods	a	E_c	C_{11}	C_{12}	C_{44}	B	G	Ref.
Empirical potential	4.556	6.235	114.6	76.5	48.9	89.2	33.5	Present
	4.545	6.439						27
	4.538	5.581						27
	4.537	6.213	102.9	67.0	38.6	79.0		32
First-principles	4.530		116.5	81.5	45.6	92.9		32
	4.405		110.9	61.2	46.1			42
	4.529							42
Exp.	4.63							44

Table 5
The calculated lattice constants (in Å), cohesive energy and mono-vacancy formation energy (in eV), elastic constants and elastic moduli (in GPa) of ω-Zr.

Methods	a	c	E_c	E_f	C_{11}	C_{12}	C_{13}	C_{33}	C_{44}	B	G	Ref.
Empirical potential	5.164	3.108	6.220	1.962[a]	185.6	98.7	54.0	152.7	14.7	102.3	30.4	Present
				1.166[b]								Present
First-principles	5.056	3.150			165.2	75.6	47.5	198.7	30.6	101.1	42.8[c]	6
					167.0	69.8	47.7	195.7	33.7			33
					161.7	72.6	53.5	195.6	33.7			45
	5.054	3.154			166.7	74.0	48.7	198.1	34.0	97.1	45.0	35
					160.9	73.7	53.6	195.1	33.8	97.4	44.7	46
Exp.	5.039	3.150										36
										90		40
										104.0	45.1	47

[a] The vacancy on the site of A plane (trigonal plane).
[b] The vacancy on the site of A plane (hexagonal plane).
[c] The value are derived from the elastic constants data reported in the corresponding references.

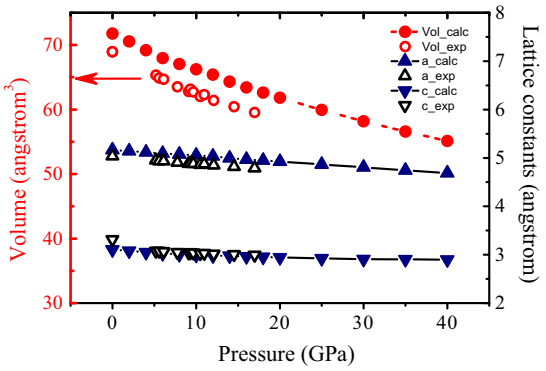

Fig. 4. The variation of unit-cell volume with pressure for ω-Zr. The experimental data taken from the Zhao et al. at temperature 973 K [40].

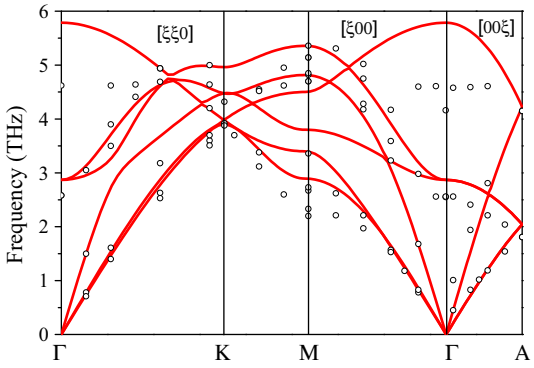

Fig. 5. Phonon dispersion curves of α-Zr. The dots are the experimental data by Stassis et al. [5].

The present dispersion spectrum is in good agreement with that of Willaime et al. [28].

We further calculated the phonon dispersion spectrum of β-Zr as demonstrated in Fig. 6, with a good agreement with experiments [5,7]. Two anomalies of phonon dispersion are reproduced. (1) The L [$\xi\xi\xi$] phonon branch has an extreme dip at $\xi = 2/3$. (2) For large ξ, the transverse [$\xi\xi$0] phonon branch (T_1) with [1 $\bar{1}$ 0] polarization is of unusual low energy. The former relates the β-to-α transformation and the latter results in the β-to-ω transformation. It is notable that the present calculated phonon dispersion indicates that bcc structure is stable at 0 K, while the first-principles [6,30] and other empirical potential [28] predicted

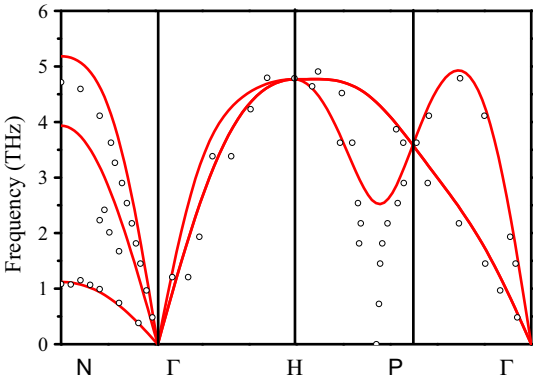

Fig. 6. Phonon dispersion curves of β-Zr. The dots are the experimental data by Stassis et al. [5].

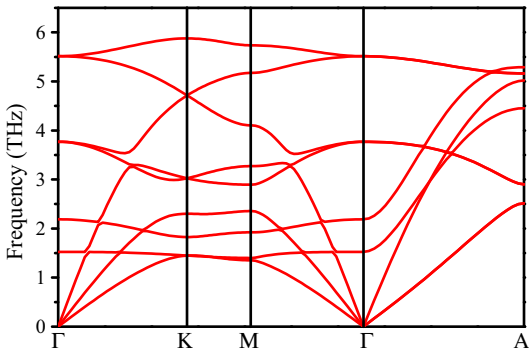

Fig. 7. Phonon dispersion curves of ω-Zr.

imaginary frequencies at N point for T_1 phonon, indicating that the bcc lattice is unstable. Herming et al. [7] have studied the temperature dependence of T_1 N-point mode by neutron scattering measurements. According to their results, the frequency appreciably decreases as the temperature approaches the β-to-α transition temperature, but the transition occurs before it completely softens.

There are no experimental data available for the high-pressure phase ω-Zr. Our phonon dispersion from la-EAM along the high-symmetry directions are displayed in Fig. 7. It is worth mentioning that Hu et al. [49] calculated the phonon dispersion curves from the first-principles and pointed that the ω phonons are expected to be stiffer along the c axis than in the basal plane due to the low c/a ratio. However, the present calculations do not confirm this characteristic.

3.4. Surface and stacking fault energy

The surface energy and stacking fault energy for α-Zr were also calculated and the results are summarized in Tables 6 and 7, respectively, along with experimental and other theoretical reports. For experimental surface energy, there are only average values for polycrystalline solids in literature. Some theoretical calculations can be performed for specific planes including the basal planes, prism planes, and pyramidal planes on demand. All of the experimental surface energy is extrapolated from high temperature experimental data through some approximation on the temperature dependence of surface energy [50]. As for the α-Zr, the calculated surface energies for basal and prism planes are less than those of experiment [50], first-principles and some potentials [18,20,27,51–56], but larger than those of other empirical potentials [17,27] and first-principles [32].

For surface energies σ, it is proportional to the surface mass density. Therefore, the planes with lower Miller indices planes have higher surface energy. For bcc crystals, the surface energies follows a general order $\sigma_{110} < \sigma_{100} < \sigma_{111}$. This order was verified in bcc Zr from our model with la-EAM potential. Our results of the surface energies for bcc Zr surfaces (1 1 0), (1 0 0) and (1 1 1) are 1273, 1454 and 1504 mJ/m^2, respectively. The present surface energies are higher than those of Bozzolo et al. [57], in which the relaxed surface energies are 522.4, 834.6 and 1254.4 mJ/m^2 for (1 0 0), (1 1 0) and (1 1 1) planes, respectively, at temperature 0 K. This discrepancy could be attribute to that the long range interactions are appropriately counted in our model. Furthermore, we are interested in the surface energies of ω-Zr. The surface energy of the planes (0 0 0 1), (1 0 $\bar{1}$ 0), (1 1 $\bar{2}$ 0) and (1 $\bar{1}$ 0 1) are 1491, 1392, 1252 and 1699 mJ/m^2, respectively. To the best of our knowledge, there is not any report of the surface energy of ω-Zr in the literature. Therefore, we are the first time to report the surface energies.

Table 6
The surface energies for low-index planes of α-Zr (in mJ/m^2).

Methods	(0 0 0 1)	(1 0 $\bar{1}$ 0)	(1 1 $\bar{2}$ 0)	(1 0 $\bar{1}$ 1)	(1 $\bar{1}$ 0 2)	Refs.
Empirical potential	1523	1327	1453	1416	1459	Present
	988		978			17
	2302		2364			18
	2156	2158	2380		2655	20
	1097		1156			23
	1270	1340		1340		27
	1540	1540		1550		27
Exp.	2050					50
First-principles	1022	1086	1230		1255	32
	1560	1640				51
	1600	1660				52
	1729					53
	2044					54
	2260	2111				55
	1600	1670		1550		56

Table 7
The stacking fault energies for α-Zr (in mJ/m^2).

Methods	I_1	I_2	E	Refs.
Empirical potential	25.4	50.1	81.5	Present
		27		16
	13	26	40	17
		62		18
		201		20
		198.6	174.6	27
	99	198	297	56
	55	110	164	56
First-principles	41	80	118	32
	124	200	249	51
		227		52
	147	213	274	56
		200	145.8	58
	168	228	300	59
Exp.		340		60

The stacking faults for critically important in determine the dislocation glides and loop-habit planes, which could be reflected by the extensive studies in α-Zr [16–18,20,27,32,51,52,56,58–60]. On the basal plane, there are two intrinsic (I_1 and I_2) and one extrinsic stacking fault. The I_1 intrinsic stacking fault is corresponding to *ABABCBCB* sequence, and I_2 has *ABABCACA* sequence. The extrinsic stacking fault E has the configuration of *ABABCABAB* sequence. Among the three stacking faults, I_2 configuration is the most important, because it is connecting with main process of plastic deformation, where one full edge dislocation splits into two Shockley partial dislocations as such process requires much lower strain energy of one full dislocation. The calculated stacking fault energies for the three possible stacking faults on the basal plane with the available values are included in Table 7. Our results agree with the literature, where the values are scattering. For example, the present calculated values are smaller than those of molecular dynamics studies [18,20,27,56], first-principles calculations [32,51,52,56,58,59] and experimental value [60], but larger than other theoretical results [16,17]. The scattering data of the stacking fault energy manifests the complexity of the defects and plasticity in Zr.

3.5. Point defect properties

There are only two types of point defects in a single element crystal, namely vacancy and self-interstitial atom (SIA). The point defects are vital in study the degradation of materials properties in irradiation, because the point defects generated during the cascade of high energy particles will diffuse, aggregate and forming clusters, dislocations, dislocation loops, voids, tetrahdrons, and other many kinds of microstructures. The evolution of defect population could significant changes in microstructures and causes a number of property changes, including mechanical, thermodynamical, electrical, and chemical properties. We will limit our study in the mono-vacancies, di-vacancies and SIA due to their prominent importance.

The mono-vacancy formation and migration energies were calculated and summarized in Table 8, along with the experimental

Table 8
Formation and migration energy of the vacancy and self-diffusion activation energies (in eV) in the basal plane and out of the plane of α-Zr.

Methods	H^f_{1v}	H^{in}_{1m}	H^{out}_{1m}	Q^{in}_{1v}	Q^{out}_{1v}	Refs.
Empirical potentials	1.70	0.86	0.96	2.52	2.62	Present
	1.86	0.775	0.785	2.635	2.645	15
	1.70	0.72	0.67	2.42	2.37	17
	1.75	0.89	0.92	2.64	2.67	23
	2.26	1.03	1.12	3.29	3.38	27
	1.67	0.63	0.72	2.30	2.39	27
	0.6	1.05	1.09	1.65	1.69	61
	1.20	1.21	1.23	2.41	2.43	61
	1.20	1.32	1.34	2.52	2.54	61
First-principles	2.07	0.54	0.65	2.61	2.72	56
	2.17	0.51	0.67	2.68	2.84	62
	2.14	0.55	0.66	2.69	2.80	62
	1.95	0.67	0.71	2.62	2.66	63
Exps.	1.36	0.98	1.02	2.35	2.38	64
	1.78–1.90	0.81–0.84	0.89–0.90			65
	1.70 [18]	0.58 ± 0.04 [67], 0.65 ± 0.05 [66], 0.65 [68]		1.975 [16], 3.6 [64], 1.20 [64], 3.31 [69], 3.17 [70]		

data and the other calculated values for comparison. Our la-EAM reproduces the experimental mono-vacancy formation energy quite well. This is surprising because we have not fit the parameters with the vacancy formation energy. The atomic migration process of a vacancy is determined by its diffusion in and out the basal planes. The migration energy of a vacancy is the energy difference between two configurations: one with an atom at the saddle point and the other that at equilibrium site. The minimum energy path describes the most energy favorable path that the mono-vacancy moves from its crystal site to the nearest vacant site. The activation energies of the mono-vacancy is a sum of formation enthalpy and migration enthalpy. Depending on the position of the vacancy, it can be defined for in basal plane diffusion: $Q^{in}_{1v} = H^{in}_{1m} + H^{f}_{1v}$ and out-off basal plane diffusion $Q^{out}_{1v} = H^{out}_{1m} + H^{f}_{1v}$. The agreement of activation energy between the present calculations and those of other calculations [15,17,23,27,56,61–64] and experiment [16,18,64–70] is reasonably well.

Vacancy diffusion mechanism is one of the most important approach for defects and microstructures evolution. Di-vacancies are expected to contribute significantly to the diffusion process because two nearby vacancies appears in the transition state of this process. They are well known to contribute the dislocation nucleation, defects clustering, and cavity formation. There are various configurations for di-vancancies. The nearest neighbor configuration means two vacancies are on two adjacent planes (denoted AB). The second-nearest neighbor configuration refers that two vacancies are in the same plane (AA). The binding energy of the di-vacancy (E^{b}_{2v}) is a function of the distance between the mono-vacancies. The binding energy of di-vacancy is defined as the formation energy difference between the two mono-vacancies and one di-vacancies: $E^{b}_{2v} = 2H^{f}_{1v} - H^{f}_{2v}$. A positive binding energy corresponds to an attractive potential between the mono-vacancies, indicating that these two mono vacancies are energetically favorable to move towards each other and form a di-vancancy. Our results from la-EAM are listed in Table 9. The present results agree well with those calculated by Hu [17] and are less than those of empirical potential [28] and first-principles [71]. Our results shows that the more compact of two-vacancy (by comparing AA and AB), the less positive the binding energy is. Interactions were seen to decrease rapidly, which implies that vacancy-vacancy should have strong binding energy and be stable, because there is energy gain in comparison to isolated mono-vacancies. We found that the di-vacancy AA and AB are much more stable than other configurations and so only the migration of these two needs be considered. We have examined four different transition states as: AB-B, AA-B, AB-A and AA-A, where the style XY-Z denotes that X and Y are the initial states, and Z is the final state of Y. It is worth pointing out that the second configuration corresponds to two different diffusion processes, but symmetrical, because the initial configuration and the final configuration are switched.

The migration energies were compared with others in Table 10. The diffusion activation energies between the AA and AB configurations is small and migration path dependent. The smallest migration energy for AB di-vacancy is almost same as for AA di-vacancy. In the case of AB, after migration of atom along the AB-B path, the di-vacancy retains the AB configuration, so continuous migration can proceed. After migration of atom along the AB-A path, the di-vacancy transfers to the AA configuration. In the case of AA, after migration of an atom along the AA-B path, the configuration of the AA di-vacancy transfers to the AB configuration. However, after migration of an atom along the AA-A path, there is a stable intermediate state, where Zr atom locates at a body-centered triangle, which is formed by the three vacancies. The atom interacts with top and bottom zirconium of neighbor plane and this configuration corresponds to a high symmetric position. Two diffusion pathways were considered during the procedure of the AA-A pathway. The migration energy of the high symmetric position is 0.66 eV larger than the other path. Our results are in agreement with previous theoretical reports on the diffusion of the di-vacancy in α-Zr [17,28,72].

The formation energy of SIA in α-Zr for eight configurations was calculated: *O, T, C, S,* B_O, B_T, B_C, and B_S, where the notation is from Johnson and Beerler [73]. As a concise introduction here, an *O* site is centered in an octahedron, a *T* site in a tetrahedron, a *C* site (crowdion) is midway between two out-off-planes nearest neighbors and *S* site is a split (dumbbell) configuration normal to the basal plane. The other four configurations denoted with B are those in the basal plane. The B_O is below an *O* site, as a projection of O to the basal plane. The B_C configuration is that the interstitial atom is

Table 9
Formation and binding energies (in eV) of di-vacancy of α-Zr.

Methods	AB		AA		Refs.
	H^{f}_{2v}	E^{b}_{2v}	H^{f}_{2v}	E^{b}_{2v}	
Empirical-potential	3.211	0.159	3.207	0.163	Present
	3.18	0.21	3.18	0.22	17
		0.236		0.248	28
First-principles	3.69	0.18	3.82	0.05	71

Table 10
The migration and diffusion activation energies of di-vacancy for α-Zr (in eV/atom).

		E^{m}_{2v}		E^{a}_{2v}		Refs.
		AB-B	AB-A	AB-B	AB-A	
AB (out of plane)	Present	0.56	0.59	3.871	3.904	Present
	Other works	0.54	0.53	3.72	3.71	17
		0.53	0.58			28
		0.52		3.44		72
AA (in plane)		AA-B	AA-A	AA-B	AA-A	
	Present	0.55	0.66	3.862	3.971	Present
	Other works	0.53	0.58	3.71	3.76	17
		0.54	0.53			28
		0.22	0.84	3.12	3.74	72

Table 11
Formation energies of various interstitial configurations for α-Zr (in eV).

Methods	O	S	C	T	Bo	Bs	Bc	Bt	Refs.
Empirical potentials	3.04	3.74	3.226	–	3.30	3.10	3.08	3.4	Present
	4.62	4.92	4.52						14
	3.57	3.57	3.60	3.57	3.58	3.51	3.52	–	17
	5.15	4.62	4.04		4.08		4.14	5.02	20
	2.80	3.04	2.78		2.63	2.51	2.50	2.80	21
	4.48		4.27		4.32				28
	4.08		3.93		3.93	3.72	3.71	3.98	74
	4.05		4.03		3.88	3.76	3.75	4.05	74
First-principles	–	4.319	3.979	–	3.97	3.76	3.756	–	29
	2.79	2.80	3.07		2.78	2.90		–	34
	2.896	3.329	3.369		2.964	3.231			75
	2.88	2.92	3.14		2.70	2.79			76
	2.98	3.17	3.37	3.17	2.82	2.96	2.82	2.82	77
	2.92	3.02			2.77	2.90			78
	2.84	3.01	3.08	–	2.88		2.95	4.03	79

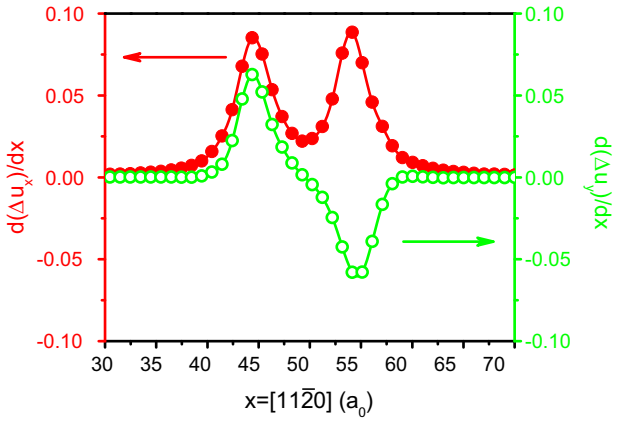

Fig. 8. The distribution of Burgers vector for 1/3[1 1 $\bar{2}$ 0](0 0 0 1) edge dislocation.

in the midway between two nearest neighbors in the basal plane. Therefore, thee atoms forms a crowdion in the dense a direction. The B_S is a split (dumbbell) configuration in the basal plane. The B_T configuration is that the interstital is just below a T site but on the basal plane. Their configurations could be refereed to, for example, Ref. [77] for details.

The formation energies of SIAs are listed in Table 11. For the SIAs in the basal plane are in general stable. The SIAs in the non-basal plane, C and O are stable. Our results are in agreement with those of Ackland [29] and Hu [17], but smaller than those calculated with other empirical potentials [14,20,28,74]. The present formation energies of SIAs are close but slightly larger than those of *ab initio* calculations [34,75–79]. As point out by Ackland [29], the non-idea c/a ratio is important in stabilizing the basal crowdion, since the basal 'nearest neighbor' are slightly farther apart than those in adjacent planes. This also can be seen from Mikhin [72].

Different potentials have yielded different SIA formation energy. The dominant effects in determining formation energy are the repulsion and the elastic constants, which describe how the strain field around the interstitial. In order to validate the present la-EAM potential further, the atomic simulation of atomic displacement for 1/3[1 1 $\bar{2}$ 0](0 0 0 1) edge dislocation has been carried out. As the study of 1/3[1 1 $\bar{2}$ 0](0 0 0 1) edge dislocation by Khater [80], the distribution of the component [b_x, b_y] of Burgers vector in the glide plane was computed. The $b_i = d(\Delta u_i)/dx$, where $\Delta(u_i)$ is the difference in the displacement component u_i between atom in atomic planes above and below the glide plane and $i = x$ or y respectively. The distribution of Burgers vector of 1/3[1 1 $\bar{2}$ 0](0 0 0 1) edge dislocation is given in Fig. 8. It can be seen that there are two peaks and the spacing of the partials is about $10a_0$, which is close to that of AWB95 potential but larger than that of MA07 potential [80]. This indicates that the present potential can reasonably describe the dislocation in α-Zr.

3.6. Phase transformations between α, β and ω phases

Martensitic (fcc) transformations are very common in nature. Due to the process-structure-property relationship, the martensitic (fcc) transformations are intentionally and widely used in engineering processing and design materials. Particularly, the $\alpha \rightarrow \omega$ transformation is the pressure driven at room temperature. It has significant technological implications, because ω phase formation lowers toughness and ductility [4] in zirconium ally. The mechanism of phase transformation, or transformation pathway for Zr has been extensively studied from theories and experiments [8,9].

The phase transition can be characterized by the orientation relationships (ORs) between the parent phase and the product phase. The ORs is important because it can be experimentally determined, providing a routine to validate the theoretical predictions. There are three possible ORs in $\alpha \rightarrow \omega$ transformation proceeds of zirconium. Usikov and Zilbershtein firstly [81] proposed composite pathway that the $\alpha \rightarrow \omega$ transformation proceeds via thermodynamically unstable β-phase under static pressure treatment, namely the transformation pathway being $\alpha \rightarrow \beta \rightarrow \omega$. The details for this transformation mechanism refereed to [8]. The other two ORs for direct transformation are described as ORI and ORII, respectively. For the pathway of ORI, (which is $(0\,0\,01)_\alpha \| (1\,\bar{2}\,1\,0)_\omega$ and $[\bar{1}\,2\,\bar{1}\,0]_\alpha \| [0\,0\,0\,1]_\omega$), each atom shuffles by 0.84 Å on the $(0\,0\,0\,1)_\alpha$ plane. The corresponding strains to produce the ω lattice was computed through a lattice relaxation of the supercells at constant volume. This configuration has hcp lattice vectors but ω lattice atomic positions The calculated strains of −3.85% along $[1\,\bar{2}\,1\,0]_\alpha$ direction, −0.34% along $[0\,0\,0\,1]_\alpha$ direction and 6.52% along $[\bar{1}\,0\,1\,0]_\alpha$ are in reasonable agreement with experimentally determined strains of −2.97%, −2.14% and 3.94% along the respective directions [82]. These are also coincident with the theoretical calculated strains of −2.22%, −2.09% and −4.46% along the respective directions [8]. The orientation relationship of ORII between α supercell and ω supercell is: $(0\,0\,0\,1)_\alpha \| (0\,1\,\bar{1}\,1)_\omega$ and $[1\,1\,\bar{2}\,0]_\alpha \| [1\,0\,\bar{1}\,1]_\omega$. This direct transformation pathway involving small atomic movement for 6 atoms in the supercell shuffles by 0.466 Å on the $(0001)_\alpha$ plane and 4 atoms out of 6 additionally shuffles by 0.509 Å out of the $(0\,0\,0\,1)_\alpha$ plane accompanied by strains of $\varepsilon_x = 0.9225$, $\varepsilon_y = 1.1234$, $\varepsilon_z = 0.9735$ produces ω supercell

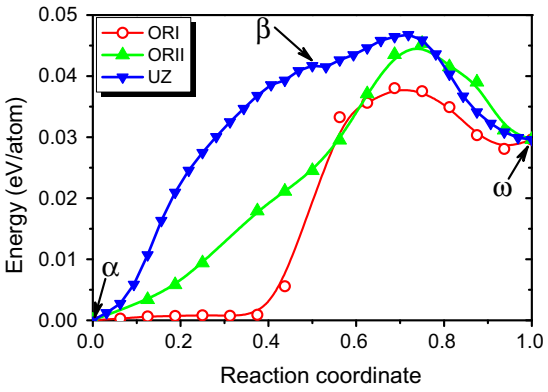

Fig. 9. Minimum potential energy versus reaction coordinate for phase transformation of Zr along three possible paths from nudged elastic band calculation.

from α. The present calculated atomic displacements and strain are in good agreement with those of tight-binding calculations [8].

The nudged elastic band is a standard method for studying of phase transition. The NEB calculations were performed by using the present la-EAM potentials employed in GULP program. The algorithm of NEB method is that it initially generates a discrete pathway with several snapshots of configurations, which directly connecting initial and final states. These snapshots of configurations are linearly interpolated according to the distance to the initial and final states. These snapshots of configurations in general has the same value. By relaxing atomic positions and lattice shape, the minimum energy path passes through the transition state. The energy barrier than can be obtained by the energy difference between the transition state and initial state. Our phase transition pathways are shown in Fig. 9, with the change in energy along $\alpha \rightarrow \omega$ transformation path for the three pathways mentioned above. One can see that ORI pathway has the lowest barrier height of 38 meV/atom compared to 45 meV/atom and 47 meV/atom for the ORII and UZ pathway, respectively. The height of energy barrier agrees well with that of tight binding calculations. However, the pathway of lowest energy barrier is ORI, while Ghosh et al. [8] predicted the lowest energy barrier is ORII. The high-pressure measurement for polycrystalline Zr using deformation-DIA methods [9,83] indicates the ORI is obeyed for both forward and reverse transformation.

It is worth noting that the two images around 0.5 in reaction coordinate of ORI route are unequally spaced, although they were initially set to be equal before the relaxation. There might be two factors causing this unprecedented jump. The first one is the asymmetry of phase transformation path ORI. The points chosen by NEB result the energy changes unevenly. One can also see from the Fig. 9, that the separation between two points are larger than others. The second reason maybe the effect of cutoff of potential. The cut off distance of the present potential is long and then more atoms are included as the deformation of phase transformation was performed. This may result in the apparent change of force and energy as numerical noise. However, the main trend and the reaction path is clearly captured.

4. Conclusions

In summary, we have developed a long-range interaction analytical EAM potential for Zr by fitting to experiments. The potential reproduces the experimentally observed *c*/*a* ratio, elastic constants, cohesive energy and monovacancy formation energy of α-Zr. The developed potential was extensively used to study the bulk, surface energy, lattice dynamic, defect properties and phase transformation for stable and metastable phases (α, β, *fcc* and ω phase) of Zr.

The calculated lattice constants and its pressure-dependence of α-Zr are in good agreement with those of experiments and first-principles. The elastic constants indicate that β-Zr is dynamic stable, agree with experiments but in contrast with the prediction from the first-principles. The calculated phonon dispersion curves for β-Zr is in good agreement with experiments.

For 0D defects, the calculated formation energy of mono-vacancy, binding energy of di-vacancy, diffusive activation energy of mono-vacancy and di-vacancy are in coincident with those of first-principles and empirical calculations. The formation energies of SIAs are also close to the first-principles calculations. For 1D defect, the distribution of Burgers vector for $1/3[1\,1\,\bar{2}\,0](0\,0\,0\,1)$ edge dislocation is similar as that of other EAM potential. For 2D defects, the calculated surface energy and stacking fault energy are slightly smaller than experimental data.

The possible mechanisms of α-ω phase transformation for Zr were studied by calculating the minimum potential energies along the three highly possible paths. The calculated energy barrier of phase-transformation is coincident with the observation of experiment. Our results indicate that the present la-EAM potential could be applied to study the thermodynamic properties and dynamic procedure of Zr.

Data availability

This la-EAM potential and associated input examples are freely available on request, in addition to the details in the following webpage: http://qpeng.org/laeam/.

Acknowledgements

This work was financially supported by the National Natural Science Foundation of China (No. 11464001, No. 51061004 and No. 51531009) and the Guangxi Natural Science Foundation of China (2014GXNSFAA118308).

References

[1] Y.K. Vohra, P.T. Spencer, Novel γ-phase of titanium metal at megabar pressures, Phys. Rev. Lett. 86 (2001) 3068–3071.
[2] S.K. Sikka, Y.K. Vohra, R. Chidambaram, Omega phase in materials, Prog. Mater. Sci. 27 (1982) 245–310.
[3] H. Xia, S.J. Duclos, A.L. Ruoff, Y.K. Vohra, New high-pressure phase transition in zirconium metal, Phys. Rev. Lett. 64 (1990) 204–207.
[4] S.A. Catledge, P.T. Spencer, Y.K. Vohra, Nanoindentation hardness and atomic force microscope imaging studies of pressure-quenched zirconium metal, Appl. Phys. Lett. 77 (2000) 3568–3570.
[5] C. Stassis, J. Zarestky, D. Arch, O.D. McMasters, B.N. Harmon, Temperature dependence of the normal vibrational modes of hcp Zr, Phys. Rev. B 18 (1978) 2632–2642.
[6] B.T. Wang, P. Zhang, H.Y. Liu, W.D. Li, P. Zhang, First-principles calculations of phase transition, elastic modulus, and superconductivity under pressure for zirconium, J. Appl. Phys. 109 (2011) 063514.1–063514.7.
[7] A. Herming, W. Petry, J. Trampenau, M. Alba, C. Herzig, H.R. Schober, G. Vogl, Phonon dispersion of the bcc phase of group-IV metals. II. bcc zirconium, a model case of dynamical precursors of martensitic transitions, Phys. Rev. B 43 (1991) 10948–10962.
[8] P.S. Ghosh, A. Arya, R. Tewari, G.K. Dey, Alpha to omega martensitic phase transformation pathways in pure Zr, J. Alloys Compds. 586 (2014) 693–698.
[9] H.X. Zong, T. Lookman, X.D. Ding, C. Nisoli, D. Brown, S.R. Niezgoda, S. Jun, The kinetics of the ω to α phase transformation in Zr, Ti: analysis of data from shock-recovered samples and atomistic simulations, Acta Mater. 77 (2014) 191–199.
[10] S. Erkoc, Empirical many-body potential energy functions used in computer simulations of condensed matter properties, Phys. Reports 278 (1997) 79–105.
[11] Y.F. Ouyang, X.P. Zhong, Interatomic potentials for computer simulation of condensed matters, Adv. Mech. 36 (2006) 321–343.
[12] M.S. Daw, M.I. Baskes, Embedded-atom method: derivation and application to impurities, surfaces, and other defects in metals, Phys. Rev. B 29 (1984) 6443–6453.

[13] M.W. Finnis, J.E. Sinclair, A simple empirical N-body potential for transition metals, Phil. Mag. A50 (1984) 45–55.
[14] D.J. Oh, R.A. Johnson, Simple embedded atom method model for fcc and hcp metals, J. Mater. Res. 3 (1988) 471–478.
[15] D.J. Oh, R.A. Johnson, Relationship between c/a ratio and point defect properties in HCP metals, J. Nucl. Mater. 169 (1989) 5–8.
[16] M. Igarashi, M. Khantha, V. Vitek, N-body interatomic potentials for hexagonal close-packed metals, Philo. Mag. B 63 (1991) 603–627.
[17] W.Y. Hu, B.W. Zhang, B.Y. Huang, F. Gao, D.J. Bacon, Analytic modified embedded atom potentials for HCP metals, J. Phys. Condens. Matter 13 (2001) 1193–1213.
[18] M.I. Baskes, R.A. Johnson, Modified embedded atom potentials for HCP metals, Model. Simul. Mater. Sci. Eng. 2 (1994) 147–163.
[19] M.I. Bakses, Modified embedded-atom potentials for cubic materials and impurities, Phys. Rev. B 46 (1992) 2727–2742.
[20] Y.M. Kim, B.J. Lee, M.I. Baskes, Modified embedded-atom method interatomic potentials for Ti and Zr, Phys. Rev. B 74 (2006) 014101.1–014101.12.
[21] R.C. Pasianot, A.M. Monti, A many body potential for α-Zr. Application to defect properties, J. Nucl. Mater. 264 (1999) 198–205.
[22] S.L. Chen, J.C. Xu, H.S. Zhang, A new scheme of many-body potentials for hcp metals, Comput. Mater. Sci. 29 (2004) 428–436.
[23] Y. Dai, J.H. Li, B.X. Liu, Long-range empirical potential model: extension to hexagonal close-packed metals, J. Phys.: Condens. Matter 21 (2009) 385402.1–385402.10.
[24] Y.F. Ouyang, X.F. Tong, C. Li, H.M. Chen, X.M. Tao, T. Hickel, Y. Du, Thermodynamic and physical properties of FeAl and Fe 3 Al: an atomistic study by EAM simulation, Physica B 407 (2012) 4530–4536.
[25] J.D. Gale, A.L. Rohl, The general utility lattice program (GULP), Molecular Simul. 29 (2003) 291–341.
[26] A. Herman, Towards a universal embedded atom method: empirically adjusted and consistent set of atomic densities for all elements of the periodic table, Int. J. Nanotechnology 2 (2005) 215–225.
[27] M.I. Mendelev, G.J. Ackland, Development of an interatomic potential for the simulation of phase transformations in zirconium, Philos. Mag. Lett. 87 (2007) 349–359.
[28] F. Willaime, C. Massobrio, Development of an N-body interatomic potential for hcp and bcc zirconium, Phys. Rev. B 43 (1991) 11653–11665.
[29] G.J. Ackland, S.J. Wooding, D.J. Bacon, Defect, surface and displacement-threshold properties of α-zirconium simulated with a many-body potential, Philos. Mag. A 71 (1995) 553–565.
[30] I. Schnell, M.D. Jones, S.P. Rudin, R.C. Albers, Tight-binding calculations of the elastic constants and phonons of hcp Zr: Complications due to anisotropic stress and long-range forces, Phys. Rev. B 74 (2006) 054104.1–054104.12.
[31] H. Ikehata, N. Nagasako, T. Furuta, A. Fukumoto, K. Miwa, T. Saito, First-principles calculations for development of low elastic modulus Ti alloys, Phys. Rev. B 70 (2004) 174113.1–174113.8.
[32] S.L. Shang, A. Saengdeejing, Z.G. Mei, D.E. Kim, H. Zhang, S. Ganeshan, Y. Wang, Z.K. Liu, First-principles calculations of pure elements: Equations of state and elastic stiffness constants, Comput. Mater. Sci. 48 (2010) 813–826.
[33] S.H. Zhang, X.Y. Zhang, Y. Zhu, S.L. Zhang, L. Qi, R.P. Liu, First-principles investigations on elastic and thermodynamic properties of zirconium under pressure, Comput. Mater. Sci. 61 (2012) 42–49.
[34] F. Willaime, Ab initio study of self-interstitials in hcp-Zr, J. Nucl. Mater. 323 (2003) 205–212.
[35] Y. Zhang, K. Luo, B.C. Yang, Z.S. Zhao, Z.Y. Liu, B. Xu, J.L. He, Y.J. Tian, D.L. Yu, Strengthening mechanism of ω-Zr, Comput. Mater. Sci. 135 (2017) 134–140.
[36] C.S. Barett, T.B. Massaski, Structure of Metals, McGram-Hill, New York, 1966.
[37] E.A. Brandes, Smithells Metal Reference Book, Butterworths, London, 1983.
[38] G. Simmons, H. Wang, Single Crystal Elastic Constants: S Handbook, MIT Press, Cambridge, MA, 1971.
[39] E.S. Fisher, C.J. Renken, Single-crystal elastic moduli and the hcp→bcc transformation in Ti, Zr, and Hf, Phys. Rev. 135 (1964) A482–A494.
[40] Y. Zhao, J. Zhang, C. Pantea, J. Qian, L.L. Daemen, P.A. Rigg, R.S. Hixson, G.T. Gray III, Y. Yang, L. Wang, Y. Wang, T. Uchida, Thermal equations of state of the α, β, and ω phases of zirconium, Phys. Rev. B 71 (2005) 1841191–1841196.
[41] A.T. Dinsdale, SGTE data for pure elements, CALPHAD 15 (1991) 317–425.
[42] X.Z. Ji, F. Jona, P.M. Marcus, Metastable tetragonal states of zirconium: theory and experiment, Phys. Rev. B 68 (2003) 075421.1–075421.5.
[43] A.R. Kaufmann, T.T. Magel, Metallurgy of Zirconium, McGraw-Hill, New York, 1955.
[44] G.E. Hill, J. Marklund, J. Martinson, B.J. Hopkins, Simultaneous LEED and RHEED studies of the growth of zirconium on the tungsten (100) surface, Surf. Sci. 24 (1971) 435–450.
[45] Y.J. Hao, L. Zhang, X.R. Chen, Y.H. Li, H.L. He, Phase transition and elastic constants of zirconium from first-principles calculations, J. Phys.: Condens. Matter 20 (2008) 235230.1–235230.5.
[46] X. Yu, R. Zhang, D. Weldon, S.C. Vogel, J. Zhang, D.W. Brown, et al., High pressure phase-transformation induced texture evolution and strengthening in zirconium metal: experiment and modeling, Sci. Rep. 5 (2015) 12552.
[47] W. Liu, B. Li, L. Wang, J. Zhang, Y. Zhao, Elasticity of ω-phase zirconium, Phys. Rev. B 76 (2007) 144107.1–144107.4.
[48] S.H. Liu, C. Stassis, K.M. Ho, Origin of the zone-center [001] LO-phonon anomaly in superconducting hcp transition metals, Phys. Rev. B 24 (1981) 5093–5097.
[49] C.E. Hu, Z.Y. Zeng, L. Zhang, X.R. Chen, L.C. Cai, Density functional study of the phase diagram and thermodynamic properties of Zr, Comput. Mater. Sci. 50 (2011) 835–840.
[50] W.R. Tyson, W.A. Miller, Surface free energies of solid metals: Estimation from liquid surface tension measurements, Surf. Sci. 62 (1977) 267–276.
[51] C. Domain, R. Besson, A. Legris, Atomic-scale ab initio study of the Zr–H system: II. Interaction of H with plane defects and mechanical properties, Acta Mater. 52 (2004) 1495–1502.
[52] Y. Udagawa, M. Yamaguchi, H. Abe, N. Sekimura, T. Fuketa, Ab initio study on plane defects in zirconium–hydrogen solid solution and zirconium hydride, Acta Mater. 58 (2010) 3927–3938.
[53] P.J. Feibelman, Relaxation of hcp (0001) surfaces: a chemical view, Phys. Rev. B 53 (1996) 13740–13746.
[54] M. Yamamoto, C.T. Chan, K.M. Ho, First-principles calculations of the surface relaxation and electronic structure of Zr (0001), Phys. Rev. B 50 (1994) 7932–7939.
[55] L. Vitos, A.V. Ruban, H.L. Skriver, J. Kollár, The surface energy of metals, Surf. Sci. 411 (1998) 186–202.
[56] C. Varvenne, O. Mackain, E. Clouet, Vacancy clustering in zirconium: an atomic-scale study, Acta Mater. 78 (2014) 65–77.
[57] G. Bozzolo, H.O. Mosca, A.M. Yacout, G.L. Hofman, Y.S. Kim, Surface properties, thermal expansion, and segregation in the U-Zr solid solution, Comput. Mater. Sci. 50 (2010) 447–453.
[58] C. Domain, Ab initio modelling of defect properties with substitutional and interstitials elements in steels and Zr alloys, J. Nucl. Mater. 351 (2006) 1–19.
[59] A. Poty, J.M. Raulot, H. Xu, J. Bai, C. Schuman, J.S. Lecomte, M.J. Philippe, C. Esling, Classification of the critical resolved shear stress in the hexagonal-close-packed materials by atomic simulation: application to α-zirconium and α-titanium, J. Appl. Phys. 110 (2011) 014905.1–14905.15.
[60] P.B. Legrand, Relations entre la structure électronique et la facilité de glissement dans les métaux hexagonaux compacts, Phil. Mag., B 49 (1984) 171–184.
[61] A.M. Monti, Diffusion Constants for the Vacancy Mechanism in Mg and α-Zr Calculation, Phys. Stat. Sol., B 167 (1991) 37–49.
[62] G. Verite, F. Willaime, C.C. Fu, Anisotropy of the vacancy migration in Ti, Zr and Hf hexagonal close-packed metals from first principles, Solid State Phenom. 129 (2007) 75–81.
[63] R.C. Pasianot, R.A. Pérez, Issues in the ab-initio assessment of hcp transition metals self-diffusion, Physica B 407 (2012) 3298–3300.
[64] J. Horváth, F. Dyment, H. Mehere, Anomalous self-diffusion in a single crystal of α-zirconium, J. Nucl. Mater. 126 (1984) 206–214.
[65] H. Wen, C.H. Woo, Temperature dependence and anisotropy of self-and mono-vacancy diffusion in α-Zr, J. Nucl. Mater. 420 (2012) 362–369.
[66] G.M. Hood, Diffusion and vacancy properties of α-Zr, J. Nucl. Mater. 139 (1986) 179.
[67] H.H. Neely, Damage rate and recovery measurements on zirconium after electron irradiation at low temperatures, Radiat. Eff. 3 (1970) 189–201.
[68] S.N. Buckley, R. Bullough, M.R. Hayns, The direct observation of irradiation damage in zirconium and its alloys, J. Nucl. Mater. 89 (1980) 283–295.
[69] G.M. Hood, Point defect diffusion in α-Zr, J. Nucl. Mater. 159 (1988) 149–175.
[70] G.M. Hood, H. Zou, R.J. Schultz, N. Matsuura, J.A. Roy, J. Jackman, Self- and Hf diffusion in α-Zr and in dilute, Fe-Free, Zr(Ti) and Zr(Nb) alloys, Def. Diff. Forum 143–147 (1997) 49–54.
[71] X.K. Xin, W.S. Lai, B.X. Liu, Point defect properties in hcp and bcc Zr with trace solute Nb revealed by ab initio calculations, J. Nucl. Mater. 393 (2009) 197–202.
[72] A.G. Mikhin, Y.N. Osetsky, V.G. Kapinos, On the anisotropic migration of point defects in hcp zirconium, Phil. Mag., A 70 (1994) 25–33.
[73] R.A. Johnson, J.R. Beerler, in: Interatomic Potentials and Crystalline Defects, AIME, New York, 1981, p. 165.
[74] C.H. Woo, H. Huang, W.J. Zhu, Low-dimension self-interstitial diffusion in α-Zr, Appl. Phys., A 76 (2003) 101–106.
[75] Q. Peng, W. Ji, H.C. Huang, S. De, Axial ratio dependence of the stability of self-interstitials in HCP structures, J. Nucl. Mater. 437 (2013) 293–296.
[76] G. Vérité, C. Domain, C.C. Fu, P. Gasca, A. Legris, F. Willaime, Self-interstitial defects in hexagonal close packed metals revisited: Evidence for low-symmetry configurations in Ti, Zr, and Hf, Phys. Rev. B 87 (2013) 134108.1–134108.6.
[77] Q. Peng, W. Ji, H.C. Huang, S. De, Stability of self-interstitial atoms in hcp-Zr, J. Nucl. Mater. 429 (2012) 233–236.
[78] G.D. Samolyuk, A.V. Barashev, S.I. Golubov, Y.N. Osetsky, R.E. Stoller, Analysis of the anisotropy of point defect diffusion in hcp Zr, Acta Mater. 78 (2014) 173–180.
[79] C. Domain, A. Legris, Ab initio atomic-scale determination of point-defect structure in hcp zirconium, Phil. Mag. 85 (2005) 569–575.
[80] H.A. Khater, D.J. Bacon, Dislocation core structure and dynamics in two atomic models of α-zirconium, Acta Mater. 58 (2010) 2978–2987.
[81] M.P. Usikov, V.A. Zibershtein, The orientation relationship between the α- and ω-phases of titanium and zirconium, Phys. Stat. Sol., A 19 (1973) 53–58.
[82] A. Rominkin, M. Talianker, O. Botsteirg, Crystallography and a model of the α→ω phase transformation in zirconium, Acta Metall. 29 (1981) 691–698.
[83] H.R. Wenk, P. Kaercher, W. Kanitpanyacharoer, E. Zepeda-Alarcon, Y. Wang, Orientation relations during the α-ω phase transition of zirconium: in situ texture observations at high pressure and temperature, Phys. Rev. Lett. 111 (2013) 195701.1–195701.5.